




Cite this: *Soft Matter*, 2017,
13, 7969

Buckling patterns in biaxially pre-stretched bilayer shells: wrinkles, creases, folds and fracture-like ridges†

Rashed Al-Rashed,^a Francisco López Jiménez,^{‡b} Joel Marthelot^b and
Pedro M. Reis  ^{*,ab}

We introduce a new experimental system to study the effects of pre-stretch on the buckling patterns that emerge from the biaxial compression of elastomeric bilayer shells. Upon fabrication of the samples, releasing the pre-stretch in the substrate through deflation places the outer film in a state of biaxial compression and yields a variety of buckling patterns. We systematically explore the parameter space by varying the pre-stretch of the substrate and the ratio between the stiffness of the substrate and film. The phase diagram of the system exhibits a variety of buckling patterns: from the classic periodic wrinkle to creases, folds, and high aspect ratio ridges. Our system is capable of readily transitioning between these buckling patterns, a first for biaxial systems. We focus on the wrinkle to ridge transition. In the latter, we find that pre-stretch plays an essential role and that the ridge geometry (width, height) remains nearly constant throughout their formation process. For the localized ridged patterns, we find that the propagation of the ridge tip depends strongly on both strain and stiffness ratio, in a way that is akin to hierarchical fracture.

Received 11th September 2017,
Accepted 9th October 2017

DOI: 10.1039/c7sm01828b

rsc.li/soft-matter-journal

1 Introduction

Self-organized surface patterning in both natural and engineered systems can often appear as a buckling instability mode of a compressed thin stiff film that is bonded to a relatively thick compliant foundation.^{1,2} This is the case, for example, in intestinal organs,³ white blood cells,⁴ and biofilms.⁵ When the film layer is subjected to a sufficient amount of compressive strain (for example through constrained film swelling,⁶ bilayer compression,⁷ or substrate pre-stretch⁸), the bilayer system becomes unstable and can exhibit a wide array of surface buckling patterns.^{9,10} Efforts to rationalize the buckling of such bilayer systems date as far back as the seminal work of Allen¹¹ in the 1960's, originally with the intent of studying skin buckling and failure of sandwich structures. More recently, the onset of surface buckling patterns has been studied in the context of thin-film material coatings, where instabilities can compromise mechanical integrity.¹²

There has been a recent shift in perspective to focus on leveraging surface buckling instabilities in applications such as smart adhesion,¹³ tunable wettability,^{14,15} aerodynamic drag control,^{16,17} microlens array fabrication,¹⁸ and biofouling control.¹⁹ In order to fully exploit the potential of bilayer systems, significant efforts have been devoted towards categorizing and quantifying the variety of the possible surface topographies,^{20,21} including patterns of wrinkles^{22–24} and creases,^{25,26} as well as more localized phenomena such as folds^{7,27,28} and ridges.^{8,29,30}

Most experimental studies on buckling patterns have been performed in uniformly flat conditions, and pre-stretch is commonly applied in a single direction, with biaxial loading being less common.^{8,31,32} Additionally, while periodic wrinkling and creasing have been studied for decades,^{11,25} other surface patterns, such as localized ridges, have only been discovered recently, and remain relatively unexplored. Ridge buckling in bilayers was first predicted theoretically only a few years ago²⁹ and has since been investigated both computationally³³ and experimentally.^{8,30} These studies showed that ridges appear through the evolution of a high amplitude localization from an initial wrinkling pattern and that a significant amount of pre-stretching of the substrate is necessary. However, there is still a timely need for more extensive experimental explorations to provide the physical insight into this class of localized buckling patterns to assist in future theoretical modeling efforts.

^a Department of Mechanical Engineering, Massachusetts Institute of Technology, Cambridge, MA 02139, USA

^b Department of Civil and Environmental Engineering, Massachusetts Institute of Technology, Cambridge, MA 02139, USA. E-mail: preis@mit.edu

† Electronic supplementary information (ESI) available. See DOI: 10.1039/c7sm01828b

‡ Present address: Ann and H.J. Smead Department of Aerospace Engineering Sciences, University of Colorado at Boulder, CO 80309, USA.

Here, we perform an experimental investigation of the phase diagram of buckling patterns of an elastic bilayer system, comprising an originally stress-free thin shell, which is bound to an elastic foundation layer that has been biaxially pre-stretched to a nearly hemispherical shape. Gradually relaxing the pre-stretch of the foundation layer imposes a state of compression in the thin shell coating, which can yield five distinct instability modes, depending on the choice of substrate pre-stretch and the stiffness ratio between the two layers. A systematic exploration of the underlying parameter space leads to a phase diagram that maps out the transitions between different surface patterns. With only moderate variations in the system and control parameters, we can transition between the various buckling patterns observed in a system under biaxial pre-stretch, which, altogether, had previously only been explored in systems with uniaxial stretching or compression.²⁰ Particular emphasis is given to studying the wrinkle-to-ridge transition and on characterizing the emergence, propagation, and morphology of the individual ridges, as well as the ensuing surface patterns. In our system, we can capture and characterize the sequential formation of the complex network of ridges as the pre-stretch of the substrate is released. We observe the process by which these ridges form and quantify parameters such as their width, height, and characteristic speed of propagation. Our analysis suggests that the propagation speed of ridges depends on both the film strain and the stiffness ratio between the film and the foundation. Interestingly, throughout the ridge formation process, their aspect ratio remains constant. Moreover, the propagation of these ridges bears analogies with hierarchical fracture of thin-film coatings.

2 Experimental apparatus and protocol

In Fig. 1a, we present a schematic diagram of the experimental protocol followed to create our samples. Photographs of the corresponding experiments are provided in Fig. 1b. First, a thick elastomeric disk is fabricated to be subsequently used as the substrate of the bilayer system. This disk is hydraulically

inflated from its initially flat configuration to a nearly hemispherical shape, thereby setting a prescribed pre-stretch.⁸ A second liquid elastomeric polymer is then poured onto the now bulged substrate, which, upon curing, results in a thin shell that is bound to the bulged pre-stretched substrate.^{34,35} The system is then slowly deflated and, as the pre-stretch is released, the film buckles to accommodate the excess in surface area.

In more detail, we fabricated flat disks of Polydimethylsiloxane (PDMS, Sylgard 184, Dow Corning), hereon referred to as the substrate, with an original radius of $R = 38$ mm and a thickness of $H = 3.25 \pm 0.15$ mm. The PDMS was cured in a convection oven at $T = 100$ °C for 10 hours. By varying the ratio of PDMS base to curing agent as {20:1, 22.5:1, 25:1}, the shear modulus of the substrate was varied as $\mu_s = \{105, 156, 191\}$ kPa. We note that we assume both layers to be incompressible, with Poisson's ratio $\nu = 0.5$. The values of μ_s were determined from independent uniaxial tensile tests (5943, Instron) of dogbone specimens. The substrate was then clamped in between two acrylic plates, ensuring that the ensemble was leak proof (Fig. 1a1). The top clamping acrylic plate contained a circular cut-out hole of radius $r_o = 25.4$ mm, through which the PDMS samples eventually protruded (Fig. 1a1 and b1). The lower acrylic plate had a smaller through hole where silicon tubing was mounted, which itself was then connected to a syringe pump (New Era Pump Systems NE-1000, Fig. 2a1). Water was then injected into the sample at a constant rate, up to a maximum prescribed volume, V_{\max} . The rise in internal pressure resulted in the PDMS disk bulging out-of-plane into a nearly spherical cap³⁶ (Fig. 1a2 and b2). The radius and subtended angle of the bulge could be precisely controlled by varying the injected volume, V_{\max} , thereby allowing control over the amount of pre-stretch imposed on the substrate.

The deformation in the substrate is quantified by the stretch ratio, defined locally as the ratio between initial and final (*i.e.*, deformed) length, $\lambda^s = L_f/L_i$. Given the symmetry of our problem, the three principal stretches are in the azimuthal, $\lambda_{\phi\phi}^s$, hoop, $\lambda_{\theta\theta}^s$, and through-the-thickness, λ_{zz}^s , directions. Our experiments provided data on two principal stretches, azimuthal and hoop stretch. Assuming full incompressibility of PDMS, the through-the-thickness stretch can be calculated as $\lambda_{zz}^s = 1/(\lambda_{\phi\phi}^s \lambda_{\theta\theta}^s)$.

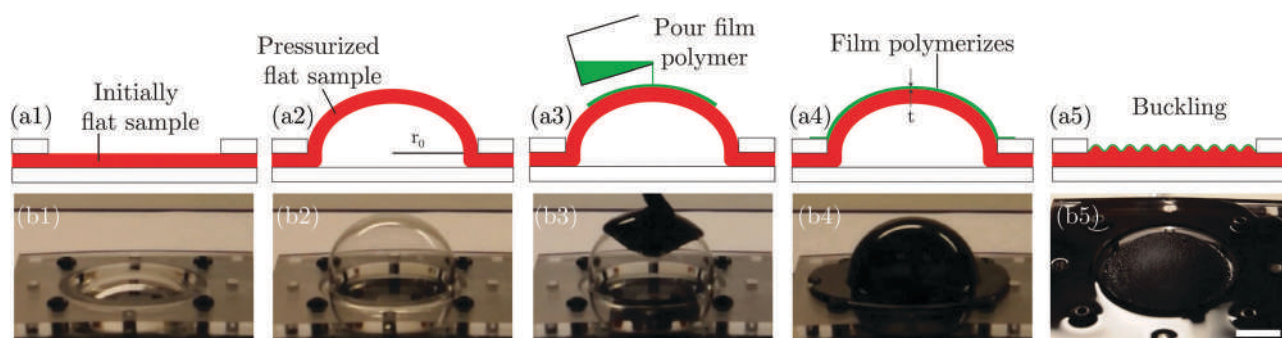


Fig. 1 (a) Schematic diagrams of the protocol followed to fabricate samples, with (b) corresponding photographs of each step of the experimental process. Samples were fabricated by first, (1) clamping the foundation layer (elastic disk) between two acrylic plates, (2) pressurizing the system to pre-stretch the disk and achieve a nearly hemispherical shape, (3) pouring a liquid polymer onto the foundation layer, which then (4) polymerizes into a thin shell coating. After depressurizing the system, (5) buckling modes are observed on the surface of the bilayer. The scale bar represents 2 cm.

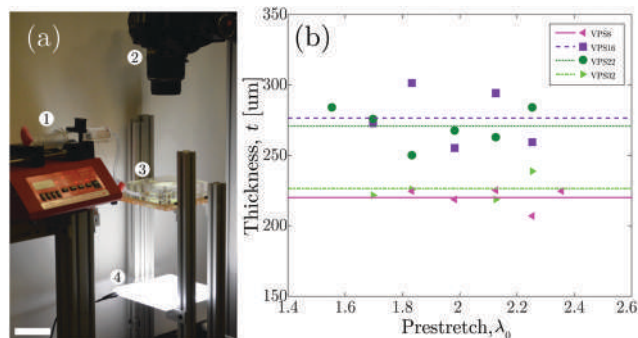


Fig. 2 (a) Photograph of the experimental apparatus, including: (1) syringe pump, (2) camera, (3) bilayer specimen, (4) light source. The scale bar represents 10 cm. (b) Thickness of the film layer obtained after pouring VPS onto substrates of varying values of pre-stretch. The horizontal lines represent the average thicknesses obtained from each polymer: VPS8, VPS16, VPS22, and VPS32 at $t_f = 220 \pm 7.8 \mu\text{m}$, $277 \pm 20 \mu\text{m}$, $271 \pm 13 \mu\text{m}$, and $226 \pm 9 \mu\text{m}$, respectively.

A calibration between the extent of inflation set by the volume of injected water, V , and the stretch of the bulged substrate disks was performed using the apparatus detailed above. The calibration process used ink markers inscribed in concentric rings along the originally flat substrate, with initial radii $r_i = \{2.7, 5.6, 8.5, 11.5\}$ mm (see Fig. 3b). The system was then steadily pressurized, and two digital SLR cameras (Nikon D3200), which were set perpendicularly to track the three-dimensional

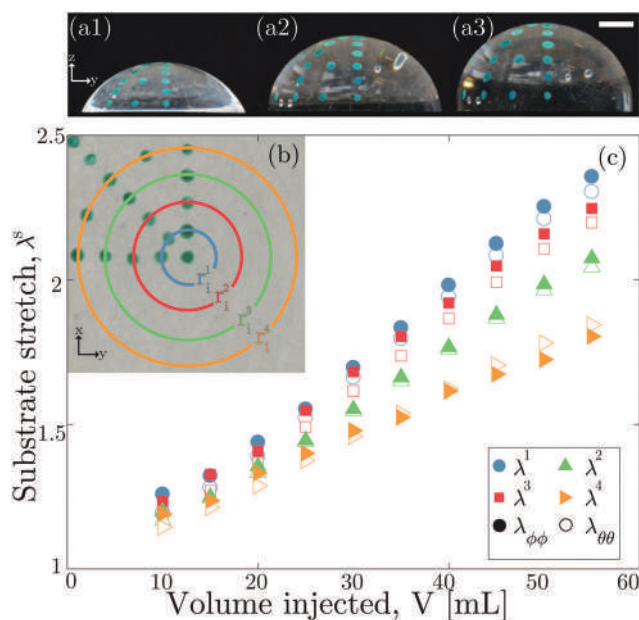


Fig. 3 (a) Set of photos showing the process by which stretch is correlated to the volume of water injected, with the three images corresponding to inflation levels of $V = 25, 40$, and 55 mL, respectively, from left to right. The scale bar represents 10 mm. (b) Top-down view of the sample in (a), along with a schematic showing the location of the markers used to measure stretch before inflation. r_0 lies at the center of the substrate, with $r_1^1 = 2.7$ mm, $r_1^2 = 5.6$ mm, $r_1^3 = 8.5$ mm, and $r_1^4 = 11.5$ mm. (c) Correlation between amount of water injected into the system, V , and the resulting substrate stretch, λ^s , for the range of $10 \leq V \leq 55$ mL. Closed symbols refer to the azimuthal stretch $\lambda_{\phi\phi}$, and open symbols to hoop stretch $\lambda_{\theta\theta}$.

positions of the markers, as seen in Fig. 3a. The hoop stretch corresponds to stretching of each of the rings, and, for the j -th marker, it was calculated as $\lambda_{\theta\theta}^{s,j} = r_f^j / r_i^j$. The azimuthal stretch corresponds to stretching between consecutive rings, calculated as $\lambda_{\phi\phi}^{s,j} = d(r_f^{j+1}, r_f^j) / (r_i^{j+1} - r_i^j)$, where $d(r_f^{j+1}, r_f^j)$ is the distance along the azimuthal arclength between rings.

The stretch-volume calibration results using the first four inner rings, spanning half the radius of the substrate, are presented in Fig. 3c; shown is the average of two independent experiments, using three markers per ring. The stretching is lower for the markers further away from the center of the bulge. The relationship between $\lambda_{\theta\theta}^s$ and $\lambda_{\phi\phi}^s$ also depends on position; changing from purely biaxial at the center (due to symmetry), to uniaxial at the boundary (where $\lambda_{\theta\theta}^s = 1$ due to the imposed boundary conditions). However, note that the stretching remains nearly biaxial in a large section of the substrate. In particular, the difference between the two principal stretches at the four points measured is below 5%. As such, the azimuthal stretch at the pole of the bulged substrate, $\lambda_{\phi\phi}^{s,1}$, can be used to define the overall stretch of the system, that we denote by λ_o . Consequently, the range of explored pre-stretch is $1.5 \leq \lambda_o \leq 2.4$, which corresponds to an injected volume of water within the range $25 \leq V_{\text{max}} [\text{mL}] \leq 55$.

In a second stage of the sample fabrication process, upon fixing V_{max} , and therefore setting the pre-stretch of the bulged substrate, a silicone-based liquid polymer, Vinyl Polysiloxane (VPS, Elite, Zhermack), was poured onto the now nearly spherical substrate (Fig. 1a3 and b3). After curing, the VPS forms a thin polymeric shell, through a viscous drainage mechanism that was studied previously by Lee *et al.*,³⁷ that is stress-free in its original configuration. Hereon, we shall refer to this VPS outer shell as the film. The thickness of this film is nearly constant, and is set by the balance between viscous draining along the substrate and curing time for VPS:³⁷ $t_f \sim \sqrt{\mu_0 R / [\rho g \tau_c]}$, where μ_0 is the characteristic viscosity of the VPS before curing, R is the radius of the mold, ρ is the density, g is acceleration due to gravity, and τ_c is the characteristic curing time.

The two parts of VPS were mixed with a 1 : 1 ratio, and left to cure at room temperature ($T = 20^\circ\text{C}$), for 1 hour. By using different polymers (Elite Double 8, 16 fast, 22, and 32; Zhermack), we were able to systematically select a variety of shear moduli, $\mu_f = \{75, 110, 194, 327\}$ kPa, and film thicknesses $t_f = \{220 \pm 7.8, 277 \pm 20, 271 \pm 13, 226 \pm 9\} \mu\text{m}$. Note that the final thickness of the shell, t_f , was systematically tuned by delaying the time between the initial mixing of the polymer solution and the moment of pouring, taking advantage of the fact that the viscosity of the polymer changes as the curing progresses.³⁷ Our results show that the type (*i.e.*, classification of the mode) of the observed buckling pattern does not vary with film thickness (within our experimentally explored range, $220 \leq t_f [\mu\text{m}] \leq 670$), as long as it is significantly smaller than that of the substrate. With that said, the characteristic length scales of the pattern do change with t_f . It is important to highlight that throughout the curing process, the stress-free film is chemically bonded to the bulged substrate (which is pre-stretched), such that no delamination occurred during the experiments.

After the VPS film cured (Fig. 1a4), the water was then withdrawn using a syringe pump at a rate of either $dV/dt = 15 \text{ mL min}^{-1}$ or 1 mL min^{-1} , both of which were slow enough for the unloading to be assumed as quasi-static. This corresponded to an approximate (de)stretch rate of $d\lambda^s/dt = -0.41 \pm 0.02 \text{ min}^{-1}$ or $-0.027 \pm 0.001 \text{ min}^{-1}$, respectively. Varying $d\lambda^s/dt$ had no observable effect on the resulting type of buckling mode, nor on the characteristic size of the resulting pattern. The unloading progressively relaxes the pre-stretch of the substrate, while simultaneously placing the film in a state of compression, leading to the emergence of a variety of surface-buckling patterns of complex topography.

The pattern formation process was imaged by a digital SLR camera (Nikon D3200, Fig. 2a2) mounted perpendicularly to and above the hemispherical sample (Fig. 2a), with the samples oriented upside-down to shield the camera from potential water damage. The resulting videos were then used to classify the buckling patterns and quantify the geometry of the patterns and their propagation process.

It is important to clarify that the undeformed state of the substrate corresponds to when it is fully deflated. On the other hand, the undeformed state of the film corresponds to the point when the VPS finishes curing (*i.e.*, when the system is fully inflated). The stretch in the film, λ^f , is then defined as a function of the stretch in the substrate and the pre-stretch, $\lambda^f = \lambda^s/\lambda_o$. However, and despite the moderate to large stretches observed in the film in our experiments, we will report its deformation using compressive strain, defined as $\varepsilon^f = 1 - \lambda^f$, as it is typically done in the relevant literature,^{14,20,38} even if ε^f is not infinitesimal.

3 Phase diagram – pattern classification

In Fig. 4, we present a phase diagram, including representative photographs, of the variety of buckling patterns observed

during the deflation of our bilayer samples. The corresponding movies of the pattern evolution are provided in ESI.† The pattern classification was performed by qualitative inspection of the obtained buckling modes. Our results show that the two primary parameters of the system are the prescribed pre-stretch, λ_o , and the stiffness ratio between the film and the substrate, $\xi = \mu_f/\mu_s$. This is in agreement with the existing literature for uniaxial stretching.²⁰ Our systematic exploration of the (λ_o, ξ) parameter space has identified the following distinct patterns: wrinkles (Fig. 4a), ridges (Fig. 4b), hierarchical ridges (Fig. 4c), creases (Fig. 4d), and folds (Fig. 4e). The presented phase diagram can be further split into two main regions based on whether the stiffness ratio is above or below unity. When the film is stiffer than the substrate ($\xi > 1$), we observe wrinkles, ridges, and hierarchical ridges, *i.e.*, buckling modes that tend to protrude outwards from the surface. When the film is softer than the substrate ($\xi < 1$), patterns of creases and folds are observed instead, both of which are directed inwards from the surface.

Let us first focus on the regime where the stiffness ratio is above unity, $\xi > 1$. Wrinkles^{22–24} (Fig. 4a, see ESI,† Movie 1) are observed for high stiffness ratios and low values of the pre-stretch ($1.55 \leq \lambda_o \leq 1.83$ and $1.02 \leq \xi \leq 3.1$). These wrinkling patterns correspond to a periodic, continuous and non-localized buckling mode. Periodic ridges^{8,29,30} (Fig. 4b, see ESI,† Movie 2) are obtained for higher values of the stiffness ratio and pre-stretch: $1.7 \leq \lambda_o \leq 1.83$ and $1.49 \leq \xi \leq 3.1$. These ridge patterns comprise localized high aspect ratio protrusions from the polymer surface. Further increasing the pre-stretch ($1.91 \leq \lambda_o \leq 2.36$ and $1.02 \leq \xi \leq 3.1$), yields hierarchical ridges (Fig. 4c, see ESI,† Movie 3), which differ from periodic ridges primarily in how they emerge at onset. Within the periodic ridge regime, large sections of the pattern tend to appear simultaneously. By contrast, hierarchical ridges appear individually and sequentially; each ridge ‘tip’ nucleates suddenly and then propagates until the ridge has fully formed. This behavior is reminiscent of a crack tip propagating on a

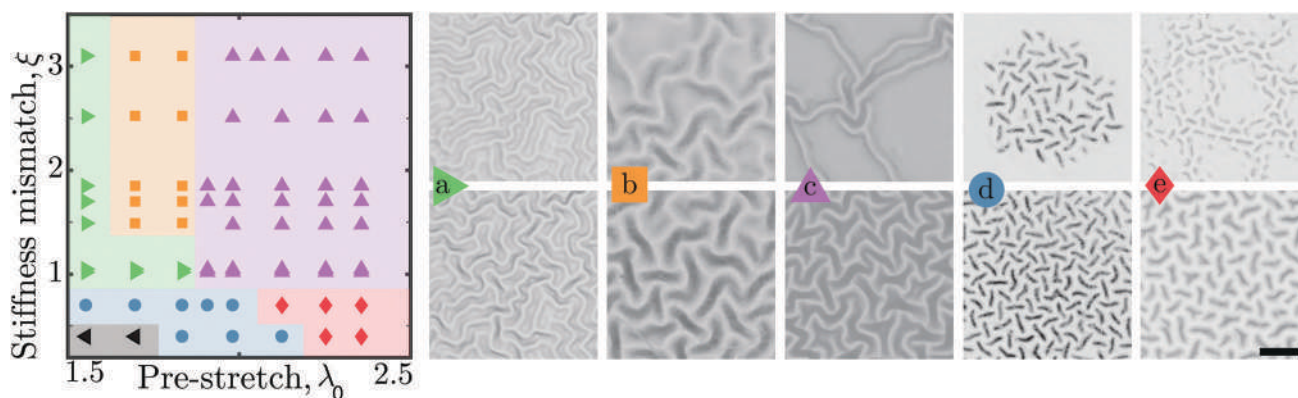


Fig. 4 Phase diagram of the different buckling patterns observed in the parameter space of pre-stretch, λ_o , and stiffness ratio, ξ : (a) wrinkles, (b) ridges, (c) hierarchical ridges, (d) creases, and (e) folds. No surface patterns are observed in the region marked with the left-facing triangles (\triangleleft). The top row of images shows typical examples of the partially formed patterns ($\varepsilon_f = 0.3 \pm 0.04$), while the bottom row represents the fully developed patterns ($\varepsilon_f = 0.36 \pm 0.06$). For a closer look at the formation of each of these patterns, please refer to ESI,† Movies 1 through 5 respectively. Darker regions within the pattern images represent areas of sharp change in height. The scale bar represents 5 mm.

brittle thin-film coating.³⁹ An analogy between these localized ridge patterns and fracture will be explored in more detail in Section 6.

When the stiffness ratio is below unity, $\xi < 1$, patterns of creases and folds form. Creases^{6,25,40} (Fig. 4d, see ESI,† Movie 4) are a surface-level buckling mode involving smaller localized perturbations directed inwards with respect to the surface, appearing at low values of pre-stretch ($1.55 \leq \lambda_o \leq 2.13$ and $0.4 \leq \xi \leq 0.7$). A crease exhibits higher local strains when compared to the rest of the surface and has a sharp tip, in contrast to wrinkles, which are characterized by a continuous surface and even strain across the film. Note that creases are highly localized cusp-like structures at their tip, and often remain within the top film layer.²⁶ Folds^{7,27,28} (Fig. 4e, see ESI,† Movie 5) are obtained at higher values of pre-stretch ($2.13 \leq \lambda_o \leq 2.36$ and $0.4 \leq \xi \leq 0.7$). Folds are a self-contacting buckling mode and, similarly to creases, are directed inwards into the substrate. The most distinguishing characteristic of folds is their tendency to penetrate into the surface and the lack of the sharp cusp that creases exhibit. At the lowest combination of stiffness ratio and pre-stretch ($1.55 \leq \lambda_o \leq 1.70$ and $\xi = 0.4$), no buckling mode was observed, and the surface of the samples remained smooth throughout deflation.

The transition between the various regions in the phase diagram of Fig. 4 is not necessarily sharp, particularly when varying the pre-stretch. For example, at low values of stiffness ratio and moderate pre-stretch (e.g., $\lambda_o = 2.1$ when transitioning from creases to folds), the observed patterns exhibit hybrid characteristics of both sides of the phase boundary. The transition between buckling modes is sharper when the stiffness ratio is varied. As such, the phase diagram presented in Fig. 4 should be regarded more as a guiding map for the relative location of the various patterns.

Similar phase diagrams have been produced in systems where the patterns result from uniaxial stretching or compression,²⁰ which show good qualitative agreement with our results. In the case of biaxial stretching, however, previous experimental studies have separately focused on a single pattern, such as wrinkles,⁴¹ folds,²⁸ or ridges.⁸ To the best of our knowledge, our experimental system is the first that can exhibit all of these buckling patterns, albeit in different regions of the parameter space.

4 Critical film strain for pattern onset

Next, we quantify the conditions for the onset of the buckling patterns in our bilayer samples during deflation. Fig. 5 shows the critical strain experienced by the film at which each specific pattern is first observed, $\epsilon_c^f = 1 - \lambda_c^f = 1 - \lambda_c^s/\lambda_o$, where λ_c^s is the stretching of the substrate at the pattern onset. In this plot, the critical film strain is shown as a function of stiffness ratio, ξ , and for different values of pre-stretch, λ_o . The data presented can again be separated into two regions, with a boundary at a stiffness ratio of unity. The most immediate observation is the apparent lack of dependence of ϵ_c on λ_o . In contrast, the critical film strain does exhibit some dependence on ξ .

At a stiffness ratio below unity ($\xi < 1$), where we observe creases and folds, we first compare our data to classical

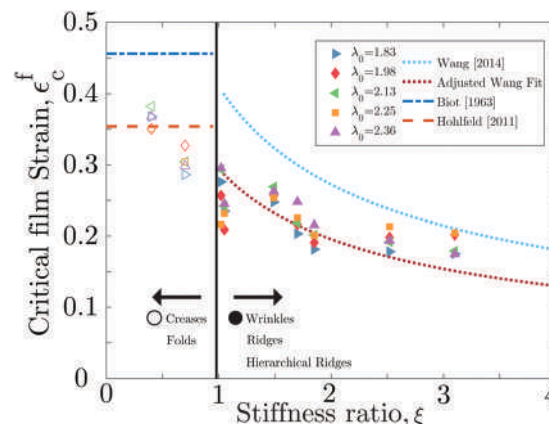


Fig. 5 Critical strain experienced by the film ϵ_c^f at which buckling patterns are first observed, as a function of stiffness ratio ξ , at various amounts of pre-stretch λ_o (see legend). Creases and folds are represented by hollow symbols at a stiffness ratio below unity, while wrinkles, ridges, and hierarchical ridges are represented by full symbols.

predictions set forth by Biot in 1963,²⁵ who calculated a critical strain of $\epsilon_c^f = 0.456$. Biot's initial analysis was purely linear, however, and did not take into account the sharp corners that are prevalent in creases. More recent nonlinear analysis and simulations² have led to an updated prediction of $\epsilon_c^f = 0.354$,⁴² which is in moderately good agreement with our experimental data presented in Fig. 5.

When the stiffness ratio is above unity ($\xi > 1$), we observe wrinkles and ridges. We now compare our data to a power-law description proposed by Wang *et al.*,²⁰ obtained through an energy scaling argument,

$$\epsilon_c^f = \alpha \xi^{-\beta}, \quad (1)$$

which has been supported by experimental data in the range $1.3 \leq \xi \leq 16$ with a prefactor of $\alpha_1 = 0.41$ and an exponent of $\beta = 0.59$. It is difficult for us to make a clear statement on the functional form of our experimental data, *vis-à-vis* eqn (1), due to the limited dynamic range. However, after fitting the prefactor of eqn (1) to our data with $\alpha_2 = 0.29 \pm 0.04$, we find moderately good agreement. We speculate that the difference between the value of the prefactor α in the study of Wang *et al.*²⁰ and our experiments could be primarily due to the difference in loading of the two studies; uni-axial stretching for theirs *versus* approximately bi-axial for ours.

Overall, the data presented in Fig. 5 establishes that the effect of the stiffness ratio ξ on the critical film strain for the onset of the patterns ϵ_c^f is far more significant than the imposed pre-stretch λ_o . For example, as ξ is increased from $\xi = 0.4$ to $\xi = 3.1$, the mean critical film strain decreases from $\epsilon_c^f = 0.364$ to $\epsilon_c^f = 0.187$, almost dropping by a factor of two. In comparison, when varying pre-stretch between $\lambda_o = 1.83$ and $\lambda_o = 2.36$, we rarely observe a variation in critical strain of more than 10%, except for $\xi = 1.05$ with a variation of 17%. We note that varying pre-stretch along the explored range includes a transition between distinct buckling modes, but with no apparent effect on critical film strain.

5 Quantification of the geometry of ridges

Having introduced and described the variety of patterns that we can achieve with our system, we highlight that ridges are the least explored out of the buckling modes presented, and are unique in that they require pre-stretch of the substrate.^{8,29} There are two other important differences between ridges and the other patterns observed in elastic bilayers. First, they have a significantly higher aspect ratio; a key parameter for many of the applications envisioned for surface patterns. Second, the mechanism for their onset is fundamentally different from most other patterns, given that ridges appear as a post-wrinkling bifurcation.

We start our detailed characterization of ridges by first quantifying their geometry. Their width and height was measured from the surface profile obtained using a 3D laser scanner (NextEngine 2020i) at various levels of deflation of the bilayer samples. In Fig. 6a, we show a representative example of the surface profile of a sample in the ridge regime (sample at $\xi = 3.1$ and $\lambda_o = 2.36$, with stretch relaxed to $\lambda^s = 1.70$, corresponding to $\epsilon^f = 0.28$). For increased clarity, a fitted sphere (constant radius) has been subtracted from the height profile data to emphasize the location and geometry of the ridges. The ridges are visible as yellow lines, corresponding to a height in the order of 1 mm with respect to the film surface. The ridges at the center of the disk do not have a preferred orientation, given that the pre-stretch stress is close to purely biaxial. On the edges of the sample, the ridges do tend to align in the circumferential direction, since the pre-stretch is mainly in the azimuthal direction. Fig. 6b shows a perspective view of the region connecting two different ridges, which appeared at different times during the nucleation process. In Fig. 6c, we then present the cross-section of one such ridge that lies on the plane perpendicular to the surface of the sample, and that passes through the dashed line in Fig. 6b. The ridge profile resembles the sinusoidal shape of an individual wavelength of the

wrinkling pattern, but as a single localized bump and with a higher aspect ratio.

To precisely quantify the ridge geometry (width, W , and height, H) we take 3D scans at different levels of deflation of a given sample. We then identify three ridges and take three cross sections for each of them. We define W as the distance between the two points where the cross section returns to the spherical profile of the bulge, and H as the difference between the highest point of the ridge and the average between the points defining W (see Fig. 6c). For both quantities, we present the average of nine measurements, \bar{W} and \bar{H} , normalized by the thickness of the film layer t_f , i.e., $\bar{w} = \bar{W}/t_f$ and $\bar{h} = \bar{H}/t_f$, respectively.

In Fig. 7a we present data for both \bar{w} and \bar{h} as a function of the film strain beyond the pattern onset, $\epsilon^f - \epsilon_c^f$, where ϵ_c^f is the critical strain at which ridges first emerge. Interestingly, past onset, both the height and width of a ridge remain approximately constant. In other words, increasing the film strain once the ridges have formed does not affect their geometry. Moreover, Fig. 7a shows that varying stiffness ratio ξ also does not affect the ridge geometry. The characteristic size

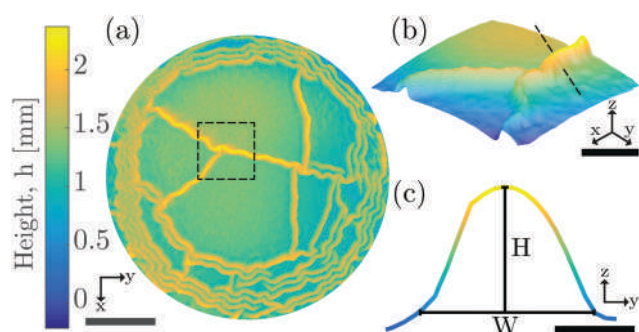


Fig. 6 (a) Topographical map of the surface of a samples obtained with a 3D laser scanner. The parameters of the sample are: $\xi = 3.1$ and $\lambda_o = 2.36$, with stretch relaxed to $\lambda^s = 1.70$, $\epsilon_f = 0.28$. The bulge's curvature has been subtracted for visual clarity, and color representing height. The scale bar represents 10 mm. (b) Zoomed-in view of a ridge network, extracted from the dashed box in (a). The scale bar represents 4 mm. (c) Cross-sectional view of a ridge, as extracted from the dashed line in (b). Schematically, H represents the ridge height, and W represents the ridge width. The scale bar represents 0.5 mm.

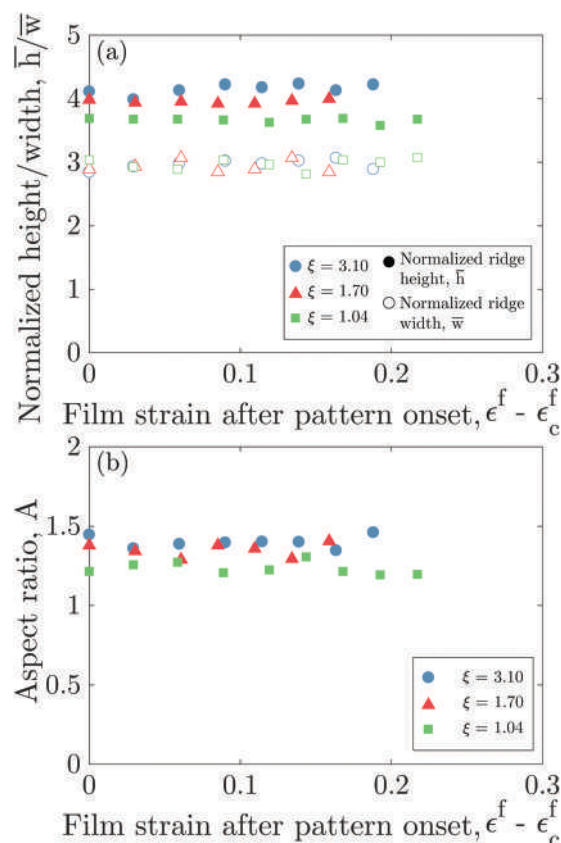


Fig. 7 (a) Normalized ridge width, $\bar{w} = W/t_f$, and normalized ridge height, $\bar{h} = H/t_f$, as functions of the film strain after the pattern onset $\epsilon^f - \epsilon_c^f$, where ϵ_c^f is the critical film strain at which ridges first emerge. The stiffness ratio ξ is varied, while all samples were held at the same value of pre-stretch ($\lambda_o = 2.36$). Increasing values along the x-axis represents deflating the sample. (b) Aspect ratio of the ridges, $A = H/W$, as a function of the strain after the pattern onset.

of a ridge is of the order of the film thickness t_f : $\bar{h} = 2.95 \pm 0.11$ and $\bar{w} = 3.93 \pm 0.09$. Consequently, for all of our data, the aspect ratio of the ridges, $A = H/W$ is constant at $A = 1.33 \pm 0.07$, throughout the deflation process. These results agree with previous experimental reports on ridge aspect ratio, despite a significant difference in stiffness ratio.⁸

Since the ridge is a localization of the wrinkle pattern, its width is expected to be similar to the wavelength of the wrinkle ℓ_w . For a linear elastic film on a pre-stretched neo-Hookean substrate, the wrinkling wavelength is:²⁹

$$\ell_w = 2\pi t_f \left(\frac{2\mu_f \lambda_o}{3\mu_s(1 + \lambda_o^3)} \right)^{1/3}. \quad (2)$$

In our experiments, we find that $W = [0.97, 0.81, 0.67] \ell_w$ for $\xi = [1.04, 1.70, 3.10]$ respectively. The fact that the ridge width is slightly smaller than the wrinkling wavelength agrees with previous experiments in a system with much larger stiffness ratio ($W/\ell_w = 0.74$ in Takei *et al.*⁸). The precise determination of the relationship between W and ℓ_w calls for new theoretical developments on the mechanism that sets the characteristic length of ridges, particularly considering bi-axial pre-stretching, which we hope that our work will motivate in the future.

6 Ridges onset and propagation

We now proceed to focus on the nucleation and propagation of hierarchical ridges, which appear as a post-wrinkling bifurcation. Specifically, as a sample is deflated and the film is subjected to an increasing state of compression, the film first develops a wrinkling pattern that is barely visible in our experiments given the associated small amplitudes and our imaging resolution. As the system is deflated further, the wrinkles become unstable and transition into localized high aspect ratio ridges.⁸ The nucleation of these ridges appears to be dominated by material imperfections, and so the precise critical compressive strain and location of each ridge presents small variations from sample to sample.

After their onset, ridges propagate along the surface, following a seemingly random path that is likely influenced by a combination of the initial wrinkling pattern and material imperfections. Due to the high aspect ratio of the ridges compared to wrinkles, they represent a localization of the compressive strain in the film,³⁰ and relax the nearby wrinkles to a flat state. The deflation of the system continuously provides an extra length of film that needs to be accommodated, resulting in the need for out-of-plane relief. This is manifested by the nucleation of new ridges, instead of an increase in the width or height of the ridges, which we showed above to remain constant during the process. As the deflation progresses, ridges appear sequentially until they cover the entire surface, at which point the network saturates and no new ridges nucleate further.

Next, we quantify the propagation speed of the ridges along the shell. For this, we use snapshots of the videos of the deflation process (see Section 2 and ESI,† Movie 6). Individual ridges are targeted, and the position of their tip is then identified on consecutive frames until the ridge propagation ceases.

The time step between different measurements is chosen according to the propagation speed and the final length of the ridge, with no less than ten snapshots taken per ridge when enough frames are available. The recorded path can then be used to calculate the speed of the ridge. Only ridges that are over a width away from other nearby ridges are considered, to avoid regions where the film strain has localized into pre-existing ridges. We note that when the system is subjected to cyclic loading beyond the initial unloading, ridges appear simultaneously upon deflation, in the same location where ridges appeared during the initial unloading. We speculate that this could be due to the highly localized stresses at the ridges, which may result in changes at the level of the polymer network, such as: crystallization, strain softening, or stress-induced diffusion of uncross-linked monomers.

In Fig. 8a we show the evolution of a representative ridge, where each point marks the position of the tip in regular 1.66 second intervals. The irregular spatial spacing between them indicates that the speed is not constant during the propagation process. This is seen more clearly in Fig. 8b, which shows the instantaneous velocity of the ridge, v , defined as the distance between each point and the next, divided by the time interval between them. The irregularity of this profile is representative of all ridges, and it is found that they can alternate periods of fast and slow propagation before finally stopping. To compare the results from several ridges, we define the mean speed v_m as the average of the instantaneous speed over the whole propagation process.

In Fig. 8c, we present the average propagation speed of ridges as a function of the representative compressive strain in

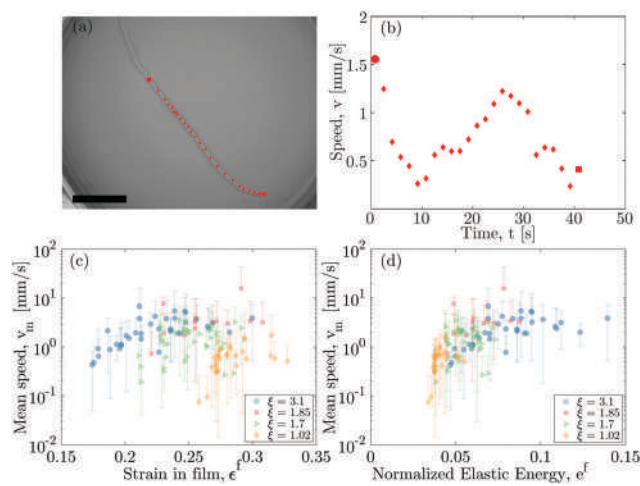


Fig. 8 (a) Photograph of a ridge. The points represent the ridge tip location at the intervals at which data was taken, at regular intervals of 50 frames (*i.e.* 1.67 seconds), displayed over the last frame in the time-lapse sequence. The larger circle represents the first measurement taken, while the square represents the last. The scale bar represents 10 mm. (b) Propagation speed of the particular ridge shown in (a), as a function of time. (c) Mean ridge propagation speed, v_m , versus the representative film strain for that ridge, ϵ^f , as stiffness ratio is varied in the range $1.02 \leq \xi \leq 3.1$. The error bars represent the standard deviation in each ridge speed time-series. (d) Same data as in (c), but plotted instead as a function of the elastic energy released by the film, normalized by the stiffness of the substrate, $\epsilon^f = \frac{1}{2}\xi(\epsilon_r^f)^2$; see eqn (3).

the film for each ridge, ϵ_r^f . This is defined as the average between the initial and final compressive strains for that ridge, $\epsilon_r^f = (\epsilon_{r,i}^f + \epsilon_{r,f}^f)/2$, defined as those at the beginning and end of the ridge propagation process, respectively. For each value of the stiffness mismatch tested (see legend of the figure), measurements were taken from all suitable ridges found across two or three samples. To relay the amount of variation in the data (as observed in Fig. 8b), we visualize the standard deviation with error bars, as seen in Fig. 8c. The data show that the ridge speed increases with the film compressive strain, despite some scatter that is likely due to the non-homogeneous strain distribution in the film, as well as the presence of material imperfections. The increase of v_m with ϵ_r^f can be attributed to the increased elastic energy within the film that is available to feed into the propagation of the ridge. The effect is more clear with earlier ridges (*i.e.*, lower strain in the film). For sufficiently high values of the film strain (*e.g.*, $\epsilon_c^f > 0.25$ for $\zeta = 3.1$) the scatter increases, while the propagation speed appears to reach a plateau. The v_m *versus* ϵ_r^f behavior also depends on the stiffness ratio between the film and the substrate. First, samples with higher stiffness mismatch nucleate earlier, as discussed in Section 4. Second, for a given value of the film strain, ridges with higher stiffness mismatch have higher propagation speeds. For example, for $\epsilon_c^f = 0.25$, the speed of the samples with $\zeta = 3.1$ is roughly one order of magnitude higher than that for the samples with $\zeta = 1.02$.

Based on the geometric invariance of the shape of the ridge (Fig. 7b) while the film strain is increased, we postulate that a fixed amount of elastic energy is released when the ridge propagates. In doing so, we were motivated by the steady-state propagation of a crack tip in the fracture of thin films bonded to an elastic substrate.⁴³ In this analogous fracture system, when the crack length is significantly larger than the film thickness, the stress field in the crack wake is invariant and independent of the crack length. Once activated, the crack does not arrest until it meets another crack or a boundary.

A rigorous derivation of the elastic energy released during ridge propagation is beyond the scope of our experimental investigation. Instead, we take an alternative point of departure that is purely empirical. Let us consider an estimation of the elastic energy released by the film when the strain in the direction perpendicular to the ridge is relaxed, normalized by the substrate stiffness:

$$e^f = \frac{1}{2}\zeta(\epsilon_c^f)^2. \quad (3)$$

In Fig. 8d we plot the mean propagation speed of the ridges as a function of e^f , and for different values of the stiffness ratio ζ . Remarkably, we find that the data collapses onto a master curve, albeit with some scatter. From the data in Fig. 8d, we see that the ridge propagation velocity appears to increase along with the amount of elastic energy stored in the film. Once sufficient elastic energy is stored, the ridge propagation velocity appears to saturate, on the order of a few mm s^{-1} . This velocity remains far below the speed of elastic waves in the substrate, which is on the order of 1000 m s^{-1} .⁴⁴ As such, the saturation of

v_m at large values of e^f does not appear to be due to inertial effects.⁴⁵ Instead, the saturation is likely connected to the time-dependent viscoelastic deformation of the substrate, in a way similar to fracture mechanics systems, such as those previously studied by Liang *et al.*⁴⁶ Confirming the validity of this interpretation will require future work.

A similar analysis using a Neo-Hookean material model to calculate the energy in the film produced nearly identical results, indicating that describing the deformation of the film using strain is a valid approximation. However, it is important to note that our rather simplistic description of ridge propagation neglects the energy in the substrate and the presence of existing wrinkled and ridged features, as well as the heterogeneity in the stretch field of the film. Nevertheless, the collapse of the data in Fig. 8d seems to indicate that this analogy between the propagation of localized ridges in pre-stretched elastic bilayers and fracture mechanics could be an interesting starting point for future studies, with a more rigorous and detailed analysis of the energetics of the system.

7 Structural hierarchy of ridge patterns

Finally, while still focusing on characterizing the patterns of ridges, we explore how the sequential nature of their onset and subsequent propagation results in hierarchical patterns. The ridges that nucleate early propagate freely along the pristine surface of the film. As the process evolves, subsequent ridges are constrained by, and often start or end at, existing ridges. To characterize this process, we have image-processed the videos of the deflation process to track the time evolution of the sequential appearance and propagation of ridges. Fig. 9a shows

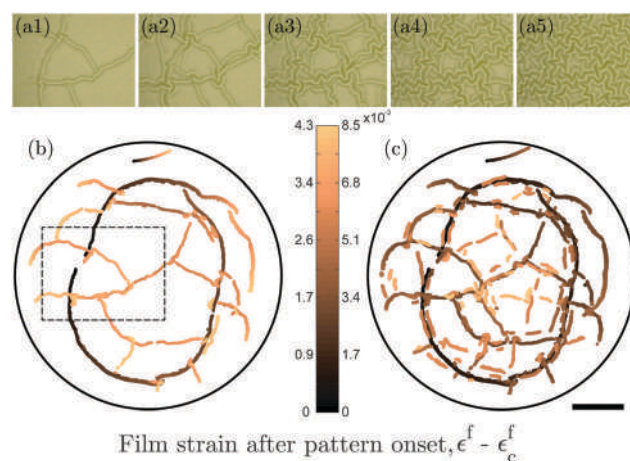


Fig. 9 (a) Snapshots of a hierarchical ridge pattern at different values of stretch, $\delta\lambda^2 = 0.077$ apart, of a sample with $\zeta = 2.52$ and $\lambda_0 = 2.36$. (b) Composite image showing the progressive appearance of ridges in the same sample presented in (a). The color bar represents film strain after the pattern onset $\epsilon^f - \epsilon_c^f$ (where ϵ_c^f is the critical film strain at which ridges first emerge). Darker colors representing earlier stages of the deflation process. The dashed rectangle corresponds to the area shown in (a). (c) Similar graph to (b), but taken with half of the sampling rate to observe later generations of ridges. The scale bar represents 10 mm, for the entire figure. Please refer to ESI,† Movie 3 for the corresponding video of the process.

successive snapshots of the deflation process of a sample with pre-stretch $\lambda_0 = 2.36$ and stiffness ratio $\xi = 1.57$, deflated at a rate of $d\lambda^s/dt = -0.41 \text{ min}^{-1}$. Each image is taken at intervals of $\delta\lambda^s = 0.077$ (i.e. approximately 11 seconds).

By repeatedly extracting pairs of consecutive frames from a given video and then subtracting them (treating each digital photograph as a grayscale 2D array), we tracked the ridge growth over time. A representative example of the results of said process is presented in Fig. 9b and c, where darker colors represent an earlier point in time. We note that the earliest ridges are longer, and typically span across a significant portion of the surface of the sample. Once a ridge has formed, it is not affected by future ridges; however, its formation is affected by the ridges preceding it. Existing ridges set the boundary conditions by which future ridges must adhere to. Later ridges tend to intersect earlier ridges, and are therefore typically shorter due to the continually decreasing amount of area where new ridges may propagate. This can be seen by comparing Fig. 9b and c, where the large, empty areas in Fig. 9b are segmented into smaller areas in Fig. 9c.

We note qualitatively that, while the change in the aspect ratio of the ridges remains constant (as discussed in Section 5), we do observe buckling of the ridges with respect to their axial direction as they are compressed by further deflation of the system. From Fig. 9a1, we see that earlier ridges appear mostly straight, with few visible kinks, while in Fig. 9a2, we later observe significant axial buckling. The amplitude of these buckles grows as the deflation continues (see Fig. 9a3–a5).

8 Discussion and conclusions

We have systematically explored the buckling patterns in a hemispherical bilayer system under hydraulic loading. Specifically, we presented a phase diagram containing buckling patterns of wrinkles, creases, folds, ridges, and hierarchical ridges. With an only moderate change in the control parameters, pre-stretch λ_0 and stiffness ratio ξ , our system can be made to transition between the various buckling patterns. Using the phase diagram as a guiding map, we then explored the effects of the parameters of the system on the critical film strain at which the film first starts to exhibit buckling. Our results indicate that increasing stiffness ratio leads to decreasing film strain while varying pre-stretch has no observable effect. We then shifted focus to the least explored of the observed buckling patterns, the ridges. Since we can slowly and incrementally increase the film strain, we first studied the wrinkle to ridge transition. Through a series of 3D scans performed at decreasing levels of system pressurization, we obtained data on normalized ridge width \bar{w} and height \bar{h} , finding that throughout the ridge formation process, the ridge geometry remains constant.

The larger scale of our system compared to previous studies^{8,20} and the subsequent ease of observation of ridge propagation has allowed us to systematically study the conditions under which their propagation speed varies. This ridge propagation speed depends strongly on both the film strain and the stiffness mismatch, a characteristic which is reminiscent of fracture in

thin-film coatings. Another similar feature with crack propagation in thin films is the observation that the ridged pattern does not appear all at the same ε . Instead, a sequential formation suggests that the propagation of the ridges in our system is dominated by a nucleation process even when the transition from wrinkles to ridges is energetically favorable, as studied in detail by Jin *et al.*³³ This hypothesis is reinforced by the fact that the ridges directly snap to a large value of amplitude (constant with strain) and a large aspect ratio of 1.33, while a slight increase of the amplitude with strain and an aspect ratio of 0.2 is expected at the onset of the transition.³³

As detailed in Section 7, the ridge formation process begins with the emergence of large, scattered ridges. As the process continues, subsequent generations of ridges have a decreasing area to grow in and are increasingly influenced by the previous generations. By way of analogy, we note that this process is reminiscent of other existing systems of localized patterns,⁴⁷ such as plant leaf vein system formation⁴⁸ and crack propagation in thin gel films,⁴⁹ where the structure of the system encodes its history. By noting the length and orientation of the ridges within the system at a given time, it is possible to deduce the temporal hierarchy of the system. This observation has also been previously made with regards to folds instead of ridges.²⁸ Beyond the insight offered into the process, further analysis of aspects such as ridge hierarchy and propagation speed could help develop a predictive model for ridge formation and connect it to other localization processes such as fracture.

Conflicts of interest

There are no conflicts to declare.

Acknowledgements

This work was supported by the National Science Foundation (CAREER CMMI-1351449).

References

- 1 M. Kücken and A. Newell, *Europhys. Lett.*, 2004, **68**, 141.
- 2 E. Hohlfield and L. Mahadevan, *Phys. Rev. Lett.*, 2011, **106**, 105702.
- 3 B. Li, Y.-P. Cao, X.-Q. Feng and H. Gao, *J. Mech. Phys. Solids*, 2011, **59**, 758–774.
- 4 L. Wang, C. E. Castro and M. C. Boyce, *Soft Matter*, 2011, **7**, 11319–11324.
- 5 M. Trejo, C. Douarche, V. Bailleux, C. Poulard, S. Mariot, C. Regeard and E. Raspaud, *Proc. Natl. Acad. Sci. U. S. A.*, 2013, **110**, 2011–2016.
- 6 J. Yoon, J. Kim and R. C. Hayward, *Soft Matter*, 2010, **6**, 5807–5816.
- 7 L. Pocivavsek, R. Dellsy, A. Kern, S. Johnson, B. Lin, K. Y. C. Lee and E. Cerda, *Science*, 2008, **320**, 912–916.
- 8 A. Takei, L. Jin, J. W. Hutchinson and H. Fujita, *Adv. Mater.*, 2014, **26**, 4061–4067.

- 9 Q. Wang and X. Zhao, *J. Appl. Mech.*, 2014, **81**, 051004.
- 10 Q. Wang and X. Zhao, *MRS Bull.*, 2016, **41**, 115–122.
- 11 H. G. Allen, *Analysis and Design of Structural Sandwich Panels: The Commonwealth and International Library: Structures and Solid Body Mechanics Division*, Elsevier, 1969.
- 12 G. Gioia and M. Ortiz, *Adv. Appl. Mech.*, 1997, **33**, 119–192.
- 13 E. P. Chan, E. J. Smith, R. C. Hayward and A. J. Crosby, *Adv. Mater.*, 2008, **20**, 711–716.
- 14 C. Cao, H. F. Chan, J. Zang, K. W. Leong and X. Zhao, *Adv. Mater.*, 2014, **26**, 1763–1770.
- 15 J. Zang, S. Ryu, N. Pugno, Q. Wang, Q. Tu, M. J. Buehler and X. Zhao, *Nat. Mater.*, 2013, 321–325.
- 16 D. Terwagne, M. Brojan and P. M. Reis, *Adv. Mater.*, 2014, **26**, 6608–6611.
- 17 M. Brojan, D. Terwagne, R. Lagrange and P. M. Reis, *Proc. Natl. Acad. Sci. U. S. A.*, 2015, **112**, 14–19.
- 18 E. P. Chan and A. J. Crosby, *Adv. Mater.*, 2006, **18**, 3238–3242.
- 19 P. Shivapooja, Q. Wang, B. Orihuela, D. Rittschof, G. P. López and X. Zhao, *Adv. Mater.*, 2013, **25**, 1430–1434.
- 20 Q. Wang and X. Zhao, *Sci. Rep.*, 2015, **5**, 1–10.
- 21 R. Zhao and X. Zhao, *J. Appl. Mech.*, 2017, **84**, 081001.
- 22 B. Audoly and A. Boudaoud, *J. Mech. Phys. Solids*, 2008, **56**, 2401–2421.
- 23 J. Song, H. Jiang, Z. Liu, D. Khang, Y. Huang, J. Rogers, C. Lu and C. Koh, *Int. J. Solids Struct.*, 2008, **45**, 3107–3121.
- 24 Y. Ebata, A. B. Croll and A. J. Crosby, *Soft Matter*, 2012, **8**, 9086–9091.
- 25 M. A. Biot, *Appl. Sci. Res.*, 1963, **12**, 168–182.
- 26 S. Cai, D. Chen, Z. Suo and R. C. Hayward, *Soft Matter*, 2012, **8**, 1301–1304.
- 27 F. Brau, P. Damman, H. Diamant and T. A. Witten, *Soft Matter*, 2013, **9**, 8177–8186.
- 28 P. Kim, M. Abkarian and H. A. Stone, *Nat. Mater.*, 2011, **10**, 952–957.
- 29 Y. Cao and J. W. Hutchinson, *J. Appl. Mech.*, 2012, **79**, 031019.
- 30 J. Zang, X. Zhao, Y. Cao and J. W. Hutchinson, *J. Mech. Phys. Solids*, 2012, **60**, 1265–1279.
- 31 S. Cai, D. Breid, A. J. Crosby, Z. Suo and J. W. Hutchinson, *J. Mech. Phys. Solids*, 2011, **59**, 1094–1114.
- 32 D. Breid and A. J. Crosby, *Soft Matter*, 2011, **7**, 4490–4496.
- 33 L. Jin, A. Takei and J. W. Hutchinson, *J. Mech. Phys. Solids*, 2015, **81**, 22–40.
- 34 D. P. Holmes and A. J. Crosby, *Adv. Mater.*, 2007, **19**, 3589–3593.
- 35 D. P. Holmes, M. Ursiny and A. J. Crosby, *Soft Matter*, 2008, **4**, 82–85.
- 36 R. Rice and S. Howell, *Am. Inst. Chem. Eng.*, 1986, **32**, 1377–1382.
- 37 A. Lee, P.-T. Brun, J. Marthelot, G. Balestra, F. Gallaire and P. M. Reis, *Nat. Commun.*, 2016, **7**, 1–11.
- 38 Y.-C. Chen and A. J. Crosby, *Adv. Mater.*, 2014, **26**, 5626–5631.
- 39 C. Allain and L. Limat, *Phys. Rev. Lett.*, 1995, **74**, 2981.
- 40 J. Kim, J. Yoon and R. C. Hayward, *Nat. Mater.*, 2010, **9**, 159–164.
- 41 N. Bowden, S. Brittain, A. G. Evans, J. W. Hutchinson and G. M. Whitesides, *Nature*, 1998, **393**, 146–149.
- 42 V. Trujillo, J. Kim and R. C. Hayward, *Soft Matter*, 2008, **4**, 564–569.
- 43 J. W. Hutchinson and Z. Suo, *Adv. Appl. Mech.*, 1991, **29**, 63–191.
- 44 J. K. Tsou, J. Liu, A. I. Barakat and M. F. Insana, *Ultrasound Interact. Biol. Med., [Proc. Int. Symp.]*, 2008, **34**, 963–972.
- 45 E. Bouchbinder, J. Fineberg and M. Marder, *Annu. Rev. Condens. Matter Phys.*, 2010, **1**, 371–395.
- 46 J. Liang, R. Huang, J. Prevost and Z. Suo, *Exp. Mech.*, 2003, **43**, 269–279.
- 47 P. M. Reis, *Nat. Mater.*, 2011, **10**, 907.
- 48 S. Bohn, B. Andreotti, S. Douady, J. Munzinger and Y. Couder, *Phys. Rev. E: Stat., Nonlinear, Soft Matter Phys.*, 2002, **65**, 061914.
- 49 Y. Couder, L. Pauchard, C. Allain, M. Adda-Bedia and S. Douady, *Eur. Phys. J. B*, 2002, **28**, 135–138.

Supplementary Material (SI) for the article:
“Buckling patterns in biaxially pre-stretched bilayer shells:
wrinkles, creases, folds and fracture-like ridges”

Rashed Al-Rashed,^a Francisco López Jiménez,^{b‡} Joel Marthelot,^b and Pedro M. Reis^{a,b}

^a*Department of Mechanical Engineering,
Massachusetts Institute of Technology,
Cambridge, MA 02139, USA*

^b*Department of Civil and Environmental Engineering,
Massachusetts Institute of Technology,
Cambridge, MA 02139, USA*

Supplementary Movies:

SI Movie 1: Representative example of the *wrinkling buckling pattern* in a sample with stiffness ratio $\xi = 3.1$ and pre-stretch $\lambda_o = 1.55$. The sample was deflated at a (de)stretch rate of $d\lambda^s/dt = -0.41$. The video was taken 30 seconds from the start of the deflation process.

SI Movie 2: Representative example of the *ridges' buckling pattern* in a sample with stiffness ratio $\xi = 1.5$ and pre-stretch $\lambda_o = 1.83$. The sample was deflated at a (de)stretch rate of $d\lambda^s/dt = -0.41$. The video was taken 60 seconds from the start of the deflation process.

SI Movie 3: Representative example of the *hierarchical ridges' buckling pattern* in a sample with stiffness ratio $\xi = 2.52$ and pre-stretch $\lambda_o = 2.36$. The sample was deflated at a (de)stretch rate of $d\lambda^s/dt = -0.41$. The video was taken 60 seconds from the start of the deflation process.

SI Movie 4: Representative example of the *creases' buckling pattern* in a sample with stiffness ratio $\xi = 0.7$ and pre-stretch $\lambda_o = 1.83$. The sample was deflated at a (de)stretch rate of $d\lambda^s/dt = -0.41$. The video was taken 75 seconds from the start of the deflation process.

SI Movie 5: Representative example of the *folds' buckling pattern* in a sample with stiffness ratio $\xi = 0.4$ and pre-stretch $\lambda_o = 2.36$. The sample was deflated at a (de)stretch rate of $d\lambda^s/dt = -0.41$. The video was taken 120 seconds from the start of the deflation process.

SI Movie 6: highlights the hierarchical nature of ridges, which is more clearly seen at a slower (de)stretch rate. The sample has a stiffness ratio $\xi = 3.1$ and pre-stretch $\lambda_o = 2.36$, and was deflated at a (de)stretch rate of $d\lambda^s/dt = -0.027$. The video was taken after the substrate stretch had relaxed to $\lambda^s = 0.425$ from the pre-stretched state.

[‡]Present address: Ann and H.J. Smead Aerospace Engineering Sciences, University of Colorado, Boulder, CO 80309, USA.